Chinese Chemical Letters 34 (2023) 108143

Contents lists available at ScienceDirect

Chinese Chemical Letters

journal homepage: www.elsevier.com/locate/cclet

Fan-like MnV_2O_6 superstructure for rechargeable aqueous zinc ion batteries

Shixian Wang[a], Yue Ru[b], Yangyang Sun[a], Huan Pang[a,*]

[a] School of Chemistry and Chemical Engineering, and Institute for Innovative Materials and Energy, Yangzhou University, Yangzhou 225009, China
[b] Interdisciplinary Materials Research Center, Institute for Advanced Study, Chengdu University, Chengdu 610106, China

ARTICLE INFO

Article history:
Received 12 November 2022
Revised 21 December 2022
Accepted 10 January 2023
Available online 13 January 2023

Keywords:
One-dimensional MnV_2O_6
Fan-nanorod superstructure
Aqueous Zn-ion batteries
Energy storage
Cathode material

ABSTRACT

In recent years, vanadate has attracted the attention of researchers for its application in electrode materials due to its high specific capacity and layered crystal structure. Herein, a typical manganese vanadium oxides (MnV_2O_6) product is efficient synthesis *via* a simple one-step hydrothermal method at 200 °C for 16 h. The as-prepared MnV_2O_6 sample is found to be the unique one-dimensional fan-like superstructure consist of several nanorods. From a microcosmic point of view, VO_6 octahedra sheets are connected by sharing edges which provides highly-open framework for rapid the intercalation and deintercalation of guest ions Therefore, stable MnV_2O_6 was prepared and used as a cathode material in aqueous zinc ion batteries, which displayed favorable specific discharge capacity, excellent coulombic efficiency and well cycling performance.

Given the growing concern over rapidly diminishing traditional fuel reserves and the serious environmental problems, sustainable energy resources such as solar and wind have come under global spotlight, which triggering the search for reliable, safe and economical electrochemical energy storage and conversion technologies [1–5]. In this case, the development of energy storage systems is essential for providing more functional and stable energy supply, and it is necessary to seek energy storage devices with strong adaptability and high efficiency [6–8]. The potential application of waterborne zinc ion batteries (ZIBs) in large-scale energy storage devices has been widely recognized. Owing to its the theoretical capacity, relatively low redox potential and stability in water due to a high overpotential for hydrogen evolution [9–13]. In recent years, as different aqueous ZIBs cathode materials have been studied and attempts have been made to improve them. However, certain problems cannot be ignored, such as unstable layered structure and low electronic conductivity, which lead to poor cycle capacity and stability. To solve these issues, many optimization strategies have been developed, such as adjusted pH to influence dendrite formation and constructed inorganic interface to suppress water decomposition *etc.* [14–16]. However, it still faces numerous challenges of serious capacity degradation and inferior rate capability [17,18]. Therefore, it is urgent to research into efficient aqueous ZIB cathode materials.

In recent years, research has focused on one-dimensional (1D) or quasi-1D nanostructures, such as nanowires, nanotubes and nanoribbons, whose shapes provide them unique physical and chemical properties that greatly broaden their potential in energy storage devices [19]. Compared to other structures the 1D nanostructure has a larger specific surface area and faster ion diffusion rate. This is very beneficial for its capacity, rate capacity and long-term cycling stability as electrode materials. However, a well-arranged array is more conducive to improving the stability of 1D nanomaterials in application to accentuate the anisotropy and conforms to the equipment design scheme. Among them, manganese vanadium oxides (MnV_2O_6) with brannerite structure as classic representative of AB_2O_6 compounds (A = Co, Mn, Mg, Zn, Cu, and B = V^{+5}) have received a great attention as an emerging electrode material due to their structural relationship with γ-MnO_2 and nonstoichiometric manganese dioxide for the battery industry [20–22]. The MnV_2O_6 compounds have been classified as monoclinic structure with a C2/*m* space group. It consists of VO_6 octahedral chains interconnected to form two parallel anion sheets, and Mn^{2+} are located between the oxygen sheets. In the event of chemical oxidation/reduction, the two metals can act as buffer substrates for each other, maintaining structural stability more effectively, which is suitable for Zn^{2+} insertion or extraction [23]. Recently, the successful synthesis of crystalline MnV_2O_6 compounds has been reported, such as solid-state reaction [24], co-precipitation [25], polymer gelation [26] and autogenous hydrothermal methods [27]. Several experiments have demonstrated

* Corresponding author.
E-mail address: huanpangchem@hotmail.com (H. Pang).

https://doi.org/10.1016/j.cclet.2023.108143
1001-8417/

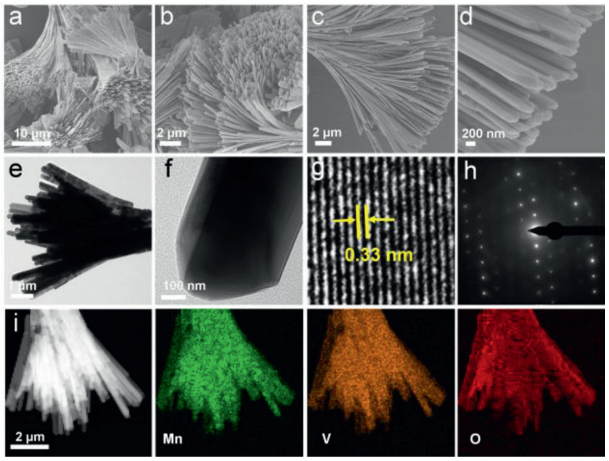

Fig. 1. The MVO-16 sample structural characterization of the as-obtained nanorods: (a-d) SEM images of different magnification; (e, f) TEM images under different magnification; (g) HRTEM image; (h) SAED pattern; (i) EDS elemental mapping images.

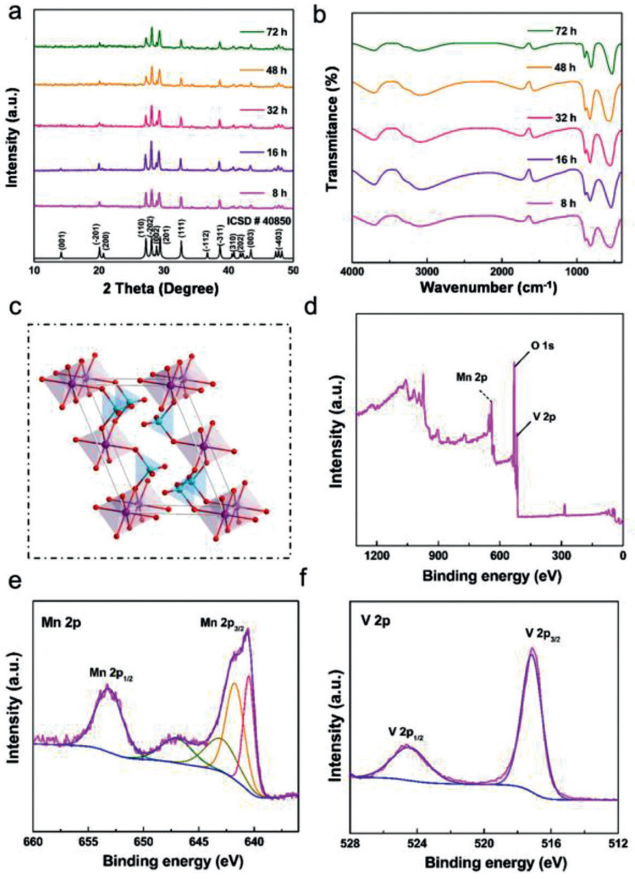

Fig. 2. (a) XRD pattern of MVO-16 sample. (b) FTIR spectrum of the as-prepared MnV_2O_6 samples for 8–72 h. (c) The schematic crystalline structure of the MnV_2O_6 unit cell from different axes. XPS spectra of the MVO-16: (d) Survey scan, (e) Mn_{2p} and (f) V_{2p}.

that the MnV_2O_6 morphology in relation to electrochemical properties is strongly influenced by the synthesis and processing methods. Often these methods are complex and require demanding reaction conditions, which leaves the product without morphological control. The hydrothermal method is considered superior to the above methods because it requires no additional heat treatment to obtain a pure crystalline phase and takes less time and effort. For instance, Huang *et al.* [19] prepared MnV_2O_6 nanobelts *via* hydrothermal route and utilized for lithium-ion batteries, which still maintain excellent cycling stability and reversible capacity under high current density.

Herein, we have synthesized MnV_2O_6 products by a facile one-pot hydrothermal method at a temperature of 200 °C for different durations. A series of 1D MnV_2O_6 are arranged together by self-arrangement to form a fan, and the interior is arranged in layers, which providing an open and flexible channel for the rapid insertion of guest ions. The electrochemical performance was investigated by fabricating a cost-effective MnV_2O_6//Zn battery utilizing MnV_2O_6 samples as the cathode material in 3 mol/L $Zn(CF_3SO_3)_2$ electrolyte. Owing to the unique 1D fan-like superstructure, the battery exhibited favorable specific discharge capacity, excellent coulombic efficiency and well cycling performance. This work provides new insights for improving the storage capacity of Zn^{2+} for practical applications.

A series of MnV_2O_6 products were prepared by a hydrothermal method at 200 °C for different hydrothermal durations from 8 h to 72 h. The products were named as MVO-X (X represent hydrothermal durations, $X = 8$, 16, 32, 48, 72). The morphology of MnV_2O_6 samples obtained from scanning electron microscopy (SEM) at different magnifications, as shown in Figs. 1a-d and Fig. S1 (Supporting information) [28]. When the reaction condition is from 8 h to 48 h, most of as-prepared the MnV_2O_6 samples demonstrate the 1D fan-like arrangements of morphology. A series of nanorods with irregular shape sizes are arrayed together to form the fan-like shapes through self-arrangement. Especially, MVO-16 samples have the most uniform size and morphology, indicating that the appropriate reaction time may have a certain influence on the homogeneous morphology of the synthesized substance. In addition, it can also be observed in Figs. S1g and h that when the reaction time was increased to 72 h, those nanorods bound together before dispersed and gradually turned to form as slender nanowires. Such phenomenon may be resulted from relatively longer reaction time. Morphology and microstructure of the as-prepared MVO-16 was further explored by the transmission electron microscopy (TEM) image of differernt magnification (Figs. 1e and f). The TEM images demostrate the uniform arrrayed nanorods exhibit the solid struture with a width of ≈400 nm for every nanorod on average. To gain further insight into the atomic-scale structure, a high-resolution TEM (HRTEM) is illustrated in Fig. 1g. The HRTEM figures of MVO-16 can be clearly seen, showing good crystallinity.The inter-planar space was measured to be 0.33 nm, which is corresponded to the (110) plane of MnV_2O_6 [29]. The fact that the nanobelts are single crystal is confirmed by the (110) plane of MnV_2O_6 parallel to the growth direction of the nanorods. At the same time, the selected area electron diffraction (SAED) diagram of a single nanorod was carried out (Fig. 1h), which proved the tip diffraction characteristics of MnV_2O_6 single crystal were consistent with the X-ray diffraction (XRD) results [21]. The elemental composition of MnV_2O_6 was further to analyze by energy dispersive X-ray spectroscopy (EDS) elemental mapping. As shown in Fig. 1i, elements Mn, V and O are uniformly distributed throughout the fan-like structure.

Fig. 2a shows the XRD patterns of all MnV_2O_6 samples for different hydrothermal durations to qualitatively analyze the phase constitution. The diffraction patterns show several characteristic diffraction peaks, which are well matched with the standard data (ICSD #40,850), indicating that crystalline all MnV_2O_6 products were successfully synthesized by the hydrothermal method. From the comparison to the standard data, there is no more peaks from other phases have been detected in the samples, which are perfectly refracted into pure monoclinic phase with the space group of C2/*m* (No. 12) and lattice constants of $a = 9.3287$ Å, $b = 3.536$ Å,

$c = 6.765$ Å and $\beta = 112.29°$ [30,31]. It can be seen that the intensity of the ($\bar{2}02$) peak was relatively strong in both samples, which means that preferential orientation makes the microcrystals have special shapes. With the extension of reaction time, the diffraction reflection intensity also increases, which indicates that the crystallinity of the samples was improved. Among them, it can be seen that the diffraction intensity of MVO-16 is relatively stronger compared to other samples, manifesting that the MnV_2O_6 sample reacted for 16 h possesses the better phase purity and crystallographic structure. From the crystal structure diagram, the internal structure of MnV_2O_6 can be more clearly understood (Fig. 2c). The interior of MnV_2O_6 structure is composed of layered structures, and each layer structure is connected by a 1D octahedral MnO_6 chain and a tetrahedral VO_4 chain. It is worth noting that these two kinds of 1D chains, each of which is extended in the form of octahedron and tetrahedron edges and corners, are linked to each other. The bond distance between Mn1-O1 and Mn1-O2 in MnO_6 chain is the same and symmetrical. On the contrary, the VO_6 complex is equipped with asymmetrical shape [25]. In fact, the distance of these V-O bonds are different. According to them, it is shown that the smallest V1-O2 bond is equal to 1.66 Å, while largest one is equal to −2.52 Å. This special V coordination can provide more possibilities for anisotropic growth, which is aligned or oriented [32]. As shown in Fig. 2b, the samples were further characterized by Fourier transform infrared spectroscopy (FTIR), and the wave number range was 80–4000 cm^{-1}. The band at 547 cm^{-1} is due to ν(V-O-V) symmetric and asymmetric stretching vibration of polymeric metavanadate [33]. The absorption band observed at 892 cm^{-1} can be ascribed to the short V-O bonds (1.665 and 1.679 Å) in MnV_2O_6 while the peak located at 795 cm^{-1} is assigned to the V-O bonds of 1.86 Å. The weak absorption peak located at 1624 cm^{-1} and the flat shoulder band at 3433 cm^{-1} may be corresponded to the bending and stretching vibrations of absorbed H_2O or hydroxyls. Based on the characterization results mentioned above, it can be concluded that the MVO-16 sample has achieved more homogeneous morphology better crystalline structure, which as it were verifies 16 h to be the better hydrothermal reaction condition.

To qualitatively evaluate the chemical compositions, the element valence states and surface energy state distribution of the compounds, X-ray photoelectron spectroscopy (XPS) test of the MnV_2O_6 samples are conducted and the results are separately shown in Figs. 2d–f, Figs. S2 and S3 (Supporting information) [28]. To take the MVO-16 sample as an example in Fig. 2d, we found the presence of Mn, V, and O elements in the samples, which can be further supported by EDS mapping.

XPS spectrum of Mn element, the binding energy at 641.6 eV corresponds to Mn $2p_{3/2}$ and the binding energy at 653.6 eV corresponds to Mn $2p_{1/2}$ (Fig. 2e) [34]. This indicates that Mn exists in the form of divalent metal cations. Besides, two peaks presented in Mn_{3s} region in the range around 82.9–89.2 eV with peak separation of 6.2 eV in Fig. S2a, further revealing the existence of Mn^{2+} as well. In the V_{2p} XPS spectrum (Fig. 2f), there are two obvious peaks at the 516.7 and 524.8 eV binding energies, respectively which are correspond to V $2p_{3/2}$ and V $2p_{1/2}$ [35]. Besides, the main peak at 530 eV can be ascribed to V-O stretch bond (Fig. S2b). The XPS analysis of other MnV_2O_6 samples MVO-X (X = 8, 32, 48, 72) shows the similar result to the MVO-16 sample in Fig. S3.

To evaluate the electrochemical performance, the coin cell-type batteries are assembled using zinc metal foil as anode, the MnV_2O_6 samples as cathode material in 3 mol/L $Zn(CF_3SO_3)_2$ solution as electrolyte at a voltage range of 0.4–1.4 V [36,37]. As shown in Fig. 3a, when the scanning rate is 0.1 mV/s, the cyclic voltammetry (CV) curves of MVO-16 for the first three cycles, which indicates that the redox reaction occurs when Zn^{2+} charge/discharge from the host framework. It is worth noting that the broad peaks on CV curves and pseudo linear voltage responses on galvanostatic charge and discharge (GCD) curves (Figs. 4a-d) mean the intercalation pseudocapacitive behavior of Zn^{2+}. In Fig. S4 (Supporting information), the CV measurement of MVO-X (X = 8, 32, 48, 72) electrodes are also carried out and the shapes are mostly similar to MVO-16 with a little difference. The CV curve (Fig. 3b) at different sweep velocities from 0.1 mV/s to 1 mV/s can more intuitively reflect the electrochemical reaction kinetics of MVO-16. With the increasing scan rate, the CV curves maintain the original curve shape and the position of the redox peaks, but there are still some slight deviations. These cyclic curves are highly coincident, indicating that the reversibility and stability of the intercalation/deintercalation process of Zn^{2+} in the Zn//MnV_2O_6 batteries. In addition, the pairs of obvious reduction and oxidation peaks can be observed, indicating that a two-step intercalation/deintercalation process of Zn^{2+} during cycling. The two cathode peaks possible represent that intercalation of Zn^{2+} into the V-O network and the reduction of MnO to Mn [38,39]. XPS characterization results showed the presence of V^{4+} and Mn^{2+}, the specific reaction equation will be introduced in the next section. The anode peak is due to the reconversion of metallic Mn and the detachment of Zn^{2+} from the host framework [23].

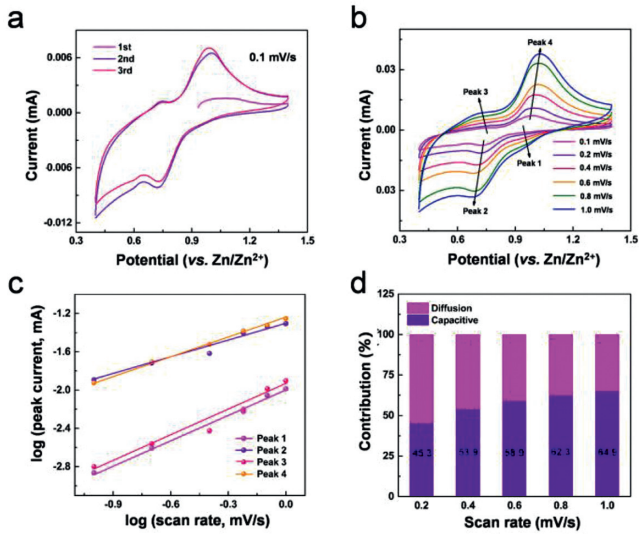

Fig. 3. Cyclic voltammetry of the MVO-16 cathode in aqueous $Zn(CF_3SO_3)_2$ electrolyte: (a) Initial three cycles of CV curves at 0.1 mV/s; (b) Typical CV curve at different scan rates of 0.1–1 mV/s; (c) log(i) *versus* log(v) plots at the cathodic current response at four peaks; (d) Separation of the capacitive and diffusion-controlled charge contributions ratios at different scan rates.

Besides, CV curves of MVO-X (X = 8, 32, 48, 72) at different scan rates of 0.1–1.0 mV/s were obtained in Figs. S4e-h. It can be observed that all shapes of the curves of the CV are almost unchanged, demonstrating the excellent reversibility of the electrochemical reactions for the MnV_2O_6 electrode. With the increase of scanning rate, the polarization increased due to the kinetic limitation of Zn^{2+} diffusion in Zn-V-O matrix, resulting in the increase of peak current gap between cathode and anode scanning. According to previous studies, the insertion and extraction mechanisms can be expressed by the following formulas [23]:

At the irreversible initial discharge process:

$$MnV_2O_6 + xZn^{2+} + 2xe^- \rightarrow Mn + Zn_xMnV_2O_6 + ZnO \quad (1)$$

Reversible charge/discharge process:

$$Mn + ZnO \leftrightarrow MnO + Zn^{2+} + 2e^- \quad (2)$$

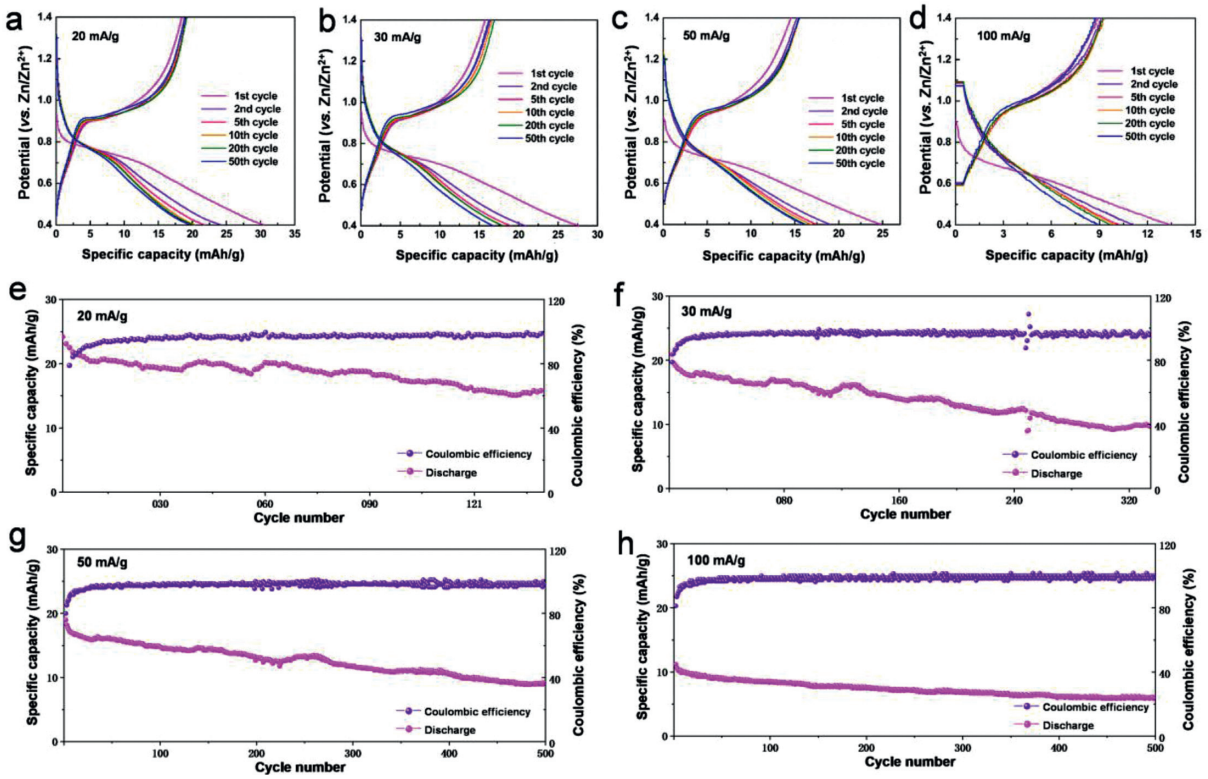

Fig. 4. (a-d) Galvanostatic charge/discharge profile of MVO-16 for different cycles at different discharge current densities of 20, 30, 50 and 100 mA/g; (e-h) Cycling performance at different discharge current densities of 20, 30, 50 and 100 mA/g.

Intercalation/deintercalation reaction:

$$Zn_xMnV_2O_6 \leftrightarrow Zn_{x-y}MnV_2O_6 + yZn^{2+} + ye^- \quad (3)$$

According to previous, the electrochemical mechanism of VO_2 in MnV_2O_6//Zn batteries is proposed [40,41]:

Anode:

$$xZn \leftrightarrow xZn^{2+} + 2xe^- \quad (4)$$

Cathode:

$$xZn^{2+} + VO_2 + 2xe^- \leftrightarrow Zn_xVO_2 \quad (5)$$

Kinetics analysis is carried out to further explore the electrochemical performance of the MVO-16 electrode and the CV curve at 0.1–1 mV/s is investigated in Fig. 3c. The relationship between the current i (mA) with the scan rate v (mV/s) is as follows:

$$i = av^b \quad (6)$$

$$\log(i) = b\log(v) + \log(a) \quad (7)$$

where a and b are constants obtained by fitting straight lines. If the $b = 0.5$, the electrochemical reaction generally indicates a diffusion-controlled intercalation, while $b = 1.0$ the electrochemical reaction suggests that the reaction is surface-limited.

According to the equation, log(i) *vs.* log(v) curves for sweep rates ranging from 0.1 mV/s to 1 mV/s can be plotted respectively, from which four redox peak b values are 0.88, 0.60, 0.89 and 0.67. According to the b value, the charge/discharge process is controlled by both ion diffusion and surface controlled reaction synergistically.The specific b values of other sapmles for different durations in Figs. S5a-d (Supporting information) were calcualted fitting in the range of 0.6–0.9, which also indicates these two forms of contribution to controll the electrochemical reaction by coordination [42]. The pseudocapacitance contribution rate of the intercalation can be calculated by the following formula [43,44]:

$$i = k_1v + k_2v^{1/2} \quad (8)$$

$$i/v^{1/2} = k_1v^{1/2} + k_2 \quad (9)$$

where k_1v and $k_2v^{1/2}$ respectively represent the contribution of capacitance and diffusion control to the total current. Combined with the formula, it is easy to fit the contribution of its capacitive current (k_1v) to the total current at different scanning rates. As shown in Fig. 3d, the contributions from pseudocapacitive reactions are 45.3%, 53.9%, 58.9%, 62.3% and 64.9% as the increasing the sweep rate from 0.1 mV/s to 1.0 mV/s. This result indicates that the battery is mainly controlled by ionic diffusion and pseudocapacitance synchronously. The electrochemical process is mainly dominated by pseudocapacitive behavior at high scan rates, which is beneficial for delivering excellent electrochemical properties [45]. Accordingly, as is depicted in Figs. S5e-h (Supporting information), the capacitive contributions of MVO-X (X = 8, 48, 72) at various scan rates are obtained to be in the range of about 32%∼58% except MVO-32, which as well manifests the control of capacitive and diffusion synergistically during the reaction. Compared the capacitive contributions of MVO-16 to other samples obtained for other time, there is a little superiority of capacitive control for MVO-16, which may be beneficial to the fast ionic migration and demonstrating better electrochemical performance [46].

The GCD was used to characterize the electrochemical performance of as-prepared MnV_2O_6 [47]. The GCD curves of MVO-16 sample for 1st, 2nd, 3rd,10th, 20th and 50th cycles at 20 mA/g were first performed in Fig. 4a [48]. Obviously, two discharge voltage plateaus appear in 0.9 V and 0.65 V. which corresponds to the re-

sult of CV curve [49]. Compared with the first cycle, discharge capacity decreases markedly from the second cycle, but both discharge and charge capacities decrease gradually afterwards and the charge capacity became even close to the discharge capacity [50,51]. To investigate the rate properties, the GCD curves at different scan rates from 20 mA/g, 30 mA/g, 50 mA/g and 100 mA/g are also conducted in Figs. 4a-d. With the charge/discharge current density increases, the initial discharge capacity of MVO-16 decreases from 30, 27.5, 25 mAh/g to 13.5 mAh/g. This phenomenon might be due to the intrinsic characteristics of MnV_2O_6 products with 1D nanorods structure, which reduced the diffusion distance of Zn^{2+} and electrons in the solid state [19]. Different discharge capacities of 24.2, 20.1 and 19.6 mAh/g were achieved MOV-16 anode after 2, 20 and 50 cycles at 20 mA/g, respectively. At the same time, with the increase of the cycles number, the discharge capacity of the MOV-16 decays slowly, indicated that MOV-16 had well cycling performance. Based on this, the GCD properties of MVO-X (X = 8, 32, 48, 72) are measured at for 1^{st}, 2^{nd}, 3^{rd},10^{th}, 20^{th} and 50^{th} cycles at different current densities in Figs. S6a-d, S7a-d, S8a-d and S9a-d (Supporting information). The initial discharge capacities are displayed to be 40, 45, 58 and 18 mAh/g, respectively, which indicates that the discharge capacities of MnV_2O_6//Zn batteries will become better the with the increase of the hydrothermal time. However, the decrease of discharge capacity of the MVO-72 may be result from the inherent influence of different material morphologies.

To further examine the cycling stability of MnV_2O_6 products, the cyclic performance of MVO-16 at different current densities are depicted in Figs. 4e-h. As shown in Fig. 4e, the battery remained the 51.4% retention of initial discharge capacity after 140 cycles and the coulombic efficiency is nearly 100% throughout the whole cycling process. As the current density raised up, the capacity degradation accordingly came to be larger, which is displayed in Figs. 4f-h. Compared to MVO-16, the cycling performance of other samples in Figs. S6e-h, S7e-h, S8e-h and S9e-h (Supporting information) displays poorer charge/discharge reversibility and long lifespan than MVO-16 which may be because of the less stable structure framework and slower ionic diffusion. However, these samples still exhibit excellent coulombic efficiency reaching almost 100%. These results indicate that the redox reaction still occurs when an irreversible transformation of the crystal structure does not generate [44].

In order to elucidate the resistance change of MVO-16 during the cyclic process at 0.1 A/g, the electrochemical impedance spectroscopy (EIS) test is performed in the frequency range of 100 kHz to 0.001 Hz in Figs. S10 and S11 (Supporting information). The impedance spectrum is composed of a semicircle in the high frequency region and an inclined straight line in the low frequency region [17]. The semicircle in the high frequency region contains the charge transfer impedance between the electrode and electrolyte. The illustration in Fig. S10 is the fitting equivalent circuit model, where R_s is the electrolyte resistance and ohmic resistances of the cell components. R_{ct} is the sum of the resistance of the charge transfer resistance of the electrochemical reaction. CPE represents the constant-phase element and Z_w represents diffusion-controlled Warburg impedance, respectively. The high-medium frequency region impedance is mainly composed of R_{ct} applied on the electrolyte/active particle interface, while the impedance in the low frequency region is composed of the corresponding diffusion barrier impedance and semi-infinite diffusion impedance [52]. The impedance of the Zn//MnV_2O_6 battery became larger after 100 cycles at 100 mA/g, which may be caused by the gradual insertion of Zn^{2+}in the reaction process. By comparsion with Fig. S10, it can be found that the impedance of MVO-16 is much smaller than other samples, which indicates a faster ion diffusion and better intercalation and deintercalation of the Zn//MnV_2O_6 battery. However, the relative large impedance should still be a problem affects the battery performance. Therefore, to further reduce the impedance the Zn//MnV_2O_6 battery in the future research is still neccessary to be improved.

In conclusion, we successfully fabricated the 1D MnV_2O_6 nanorods via a facile hydrothermal reaction at a temperature of 200 °C for different duration and obtained MnV_2O_6 nanorods with uniform fan-like superstructure for 16 h. These products were used as the cathode material for aqueous MnV_2O_6//Zn batteries in 3 mol/L $Zn(CF_3SO_3)_2$ solution at a voltage range of 0.4–1.4 V. The MnV_2O_6 structure is arranged in layer network while each layer consists of octahedral MnO_6 chains and tetrahedral VO_4 chains, which provides open and flexible channels for Zn^{2+} transfer. Taken advantage of such superstructure, the assembled MnV_2O_6//Zn battery exhibited favorable specific discharge capacity, excellent coulombic efficiency, and well cycling performance. Therefore, this investigation proved the metal vanadate material has great potential for ZIBs. Since the electrochemical performance of vanadate is highly dependent on interlayer cations, doping or substituting cations is a promising strategy to further improve the electrochemical performance of ZIBs. This study provides a new choice in the future for high-performance electrodes and has great potential for building the next generation energy storage devices.

Declaration of competing interest

The authors declare that they have no known competing financial interests or personal relationships that could have appeared to influence the work reported in this paper.

Acknowledgments

This work was supported by the National Natural Science Foundation of China (No. U1904215), the Natural Science Foundation of Jiangsu Province (No. BK20200044), and the Changjiang Scholars Program of the Ministry of Education (No. Q2018270).

Supplementary materials

Supplementary material associated with this article can be found, in the online version, at doi:10.1016/j.cclet.2023.108143.

References

[1] D. Kundu, B.D. Adams, V. Duffort, S.H. Vajargah, L.F. Nazar, Nat. Energy 1 (2016) 16119.
[2] X. Guo, H. Xu, W. Li, et al., Adv. Sci. 10 (2022) 2206084.
[3] T. Chen, F. Wang, S. Cao, et al., Adv. Mater. 34 (2022) 2201779.
[4] M. Du, P. Geng, C. Pei, et al., Angew. Chem. Int. Ed. 61 (2022) e202209350.
[5] Q. Zhang, J. Luan, Y. Tang, X. Ji, H. Wang, Angew. Chem. Int. Ed. 59 (2020) 13180–13191.
[6] S. Liu, L. Kang, J.M. Kim, et al., Adv. Energy Mater. 10 (2020) 2000477.
[7] D. Chen, M. Lu, D. Cai, et al., J. Energy Chem. 54 (2021) 712–726.
[8] J. Gu, Y. Peng, T. Zhou, et al., Nano Res. Energy 1 (2022) e9120009.
[9] W. Sun, F. Wang, B. Zhang, et al., Science 371 (2021) 46–51.
[10] S. Zheng, Y. Sun, H. Xue, et al., Natl. Sci. Rev. 9 (2022) nwab197.
[11] L. Zeng, H. He, H. Chen, et al., Adv. Energy Mater. 12 (2022) 2103708.
[12] L. Zeng, J. He, C. Yang, et al., Energy Storage Mater 54 (2023) 469–477.
[13] X. Guo, W. Li, Q. Zhang, et al., Chem. Eng. J. 432 (2022) 134413.
[14] Q. Yang, N. Jiang, Y. Shao, et al., Sci. China Chem. 65 (2022) 2351–2368.
[15] Q. Yang, L. Li, T. Hussain, D. Wang, et al., Angew. Chem. Int. Ed. 61 (2022) e202206471.
[16] Q. Yang, X. Qu, H. Cui, et al., Angew. Chem. Int. Ed. 61 (2022) e202112304.
[17] J. Hao, L. Yuan, B. Johannessen, et al., Angew. Chem. Int. Ed. 133 (2021) 25318–25325.
[18] J. Hao, L. Yuan, Y. Zhu, M. Jaroniec, S. Qiao, Adv. Mater. 34 (2022) 2103708.
[19] W. Huang, S. Gao, X. Ding, L. Jiang, M. Wei, J. Alloys Compd. 495 (2010) 185–188.
[20] J.I. Viegas, R.L. Moreira, A. Dias, Cryst. Growth Des. 19 (2019) 3233–3243.
[21] W. Zhang, L. Shi, K. Tang, Z. Liu, Mater. Res. Bull. 47 (2012) 1725–1733.
[22] N. Khamaru, S. De, A. Das, et al., Magn. Mater. 497 (2020) 165995.
[23] R. Muruganantham, W.R. Liu, C.H. Lin, M. Rudysh, M. Piasecki, J. Energy Storage 26 (2019) 100915.

[24] X. Wu, W. Wu, X. Cui, S. Liao, J. Therm. Anal. Calorim. 109 (2012) 163–169.
[25] S. Kim, H. Ikuta, M. Wakihara, Solid State Ionics 139 (2001) 57–65.
[26] T. Morishita, K. Nomura, T. Inamasu, M. Inagaki, Solid State Ionics 176 (2005) 2235–2241.
[27] Y. Wu, Z. Zhu, Y. Li, et al., Small 17 (2021) 2008182.
[28] P. Geng, L. Wang, M. Du, et al., Adv. Mater. 34 (2022) 2107836.
[29] Y. Liu, Y. Zhang, J. Du, W. Yu, Y. Qian, J. Cryst. Growth 291 (2006) 320–324.
[30] F. Wan, S. Huang, H. Cao, et al., ACS Nano 14 (2020) 6752–6760.
[31] N. Wen, S. Chen, Q. Lu, et al., Nanoscale 14 (2022) 10428–10438.
[32] K.H. Kim, Y.H. Choi, S.H. Hong, Nanoscale 12 (2020) 16028–16033.
[33] M. N, S. V, Chem. Phys. Lett. 737 (2019) 136832.
[34] Z. Li, Y. Ren, L. Mo, et al., ACS Nano 14 (2020) 5581–5589.
[35] C. Liu, Z. Neale, J. Zheng, et al., Energy Environ. Sci. 12 (2019) 2273–2285.
[36] Y. Li, Z. Wang, Y. Cai, et al., Energy Environ. Mater. 5 (2022) 823–851.
[37] N. Zhang, F. Cheng, Y. Liu, et al., J. Am. Chem. Soc. 138 (2016) 12894–12901.
[38] S. Deng, H. Li, B. Chen, et al., Chem. Eng. J. 452 (2023) 139115.
[39] X. Liu, T. Cao, S. Li, et al., J. Power Sources 525 (2022) 321134.
[40] X. Zhang, X. Li, F. Jiang, et al., Dalt. Trans. 49 (2020) 1794–1802.
[41] Y. Liu, T. Lv, H. Wang, et al., Chem. Eng. J. 417 (2021) 128408.
[42] T. Lv, G. Zhu, S. Dong, et al., Angew. Chem. Int. Ed. (2022) e202216089.
[43] B. Yan, X. Li, X. Fu, et al., Nano Energy 78 (2020) 105233.
[44] Z. Pan, J. Yang, J. Yang, et al., ACS Nano 14 (2020) 842–853.
[45] F. Wan, L. Zhang, X. Dai, et al., Nat. Commun. 9 (2018) 1656.
[46] H. Geng, M. Cheng, B. Wang, et al., Adv. Funct. Mater. 30 (2020) 1907684.
[47] C. Zhu, G. Fang, S. Liang, et al., Energy Storage Mater 24 (2020) 394–401.
[48] S. Zhang, R. Hu, L. Liu, D. Wang, Mater. Lett. 124 (2014) 57–60.
[49] S. Huang, F. Wan, S. Bi, et al., Angew. Chem. Int. Ed. 58 (2019) 4313–4317.
[50] M. Inagaki, T. Morishita, M. Hirano, V. Gupta, Solid State Ionics 156 (2003) 275–282.
[51] S. Lei, K. Tang, Y. Jin, C. Chen, Nanotechnology 18 (2007) 175605.
[52] X. Wang, F. Wang, L. Wang, et al., Adv. Mater. 28 (2016) 4904–4911.